Chemical Engineering Journal 499 (2024) 155885

Contents lists available at ScienceDirect

Chemical Engineering Journal

journal homepage: www.elsevier.com/locate/cej

Bijel-based mesophotoreactor with integrated carbon nitride for continuous-flow photocatalysis

Nicolò Allasia [a], Oleksii Nevskyi [b], Marcello Marelli [c], Igor Plazl [d], Jody Albertazzi [a], Valentina Busini [a], Franca Castiglione [a], Filippo Rossi [a], Gianvito Vilé [a,*]

[a] Department of Chemistry, Materials, and Chemical Engineering "Giulio Natta", Politecnico di Milano, Piazza Leonardo da Vinci 32, 20133 Milano, Italy
[b] Faculty of Physics, Georg August University of Göttingen, Friedrich-Hund-Platz 1, 37077 Göttingen, Germany
[c] Istituto di Scienze e Tecnologie Chimiche "Giulio Natta", Consiglio Nazionale delle Ricerche (CNR), via Gaudenzio Fantoli 16, 20138 Milano, Italy
[d] Faculty of Chemistry and Chemical Technology, University of Ljubljana, Večna pot 113, 1000 Ljubljana, Slovenia

ARTICLE INFO

Keywords:
Flow chemistry
Heterogeneous catalysis
Polymeric microreactors
Process scale up
Porous architecture

ABSTRACT

The integration of continuous-flow technologies with heterogeneous photocatalysis has recently emerged as a promising strategy for the development of sustainable processes. Although conventional packed bed reactors have been extensively utilized in industrial catalytic applications, they face challenges related to energy transfer in the photocatalytic systems. This study presents an innovative approach to address this issue by integrating heterogeneous photocatalysts with an organic polymer, leading to the fabrication of a mesophotoreactor featuring a bijel-based structural configuration. This novel strategy involves hybridizing polypentadecalactone and *in situ* confining of carbon nitride in a bicontinuous porous mesoarchitecture. The structural and physicochemical properties of the resulting catalytic composite material are evaluated through an array of characterization methods, affirming the successful integration of carbon nitride within the overall structure. The unique bicontinuous porous architecture of the composite and its suitability for industrial applications is verified, as exemplified by its exceptional efficiency in the photodegradation of methylene blue (>99 %) under flow conditions and remarkable stability up to three reaction cycles. A mathematical model is developed to describe continuous photocatalytic processes occurring in the novel tubular mesophotoreactor, with a specific focus on the degradation of the methylene blue dye. This model is successfully validated, leading to results in agreement with the experimental measurements. Additionally, fluid dynamics simulations demonstrate that the mesophotoreactor design allows for the effective diffusion of light through its channels, resulting in higher irradiation levels compared to conventional systems such as packed bed reactors. The innovative design of the catalytic reactor presented in this work offers a versatile and efficient alternative to the conventional heterogeneous systems, significantly broadening the range of applications for photocatalytic processes.

1. Introduction

Heterogeneous photocatalysis has emerged as a powerful tool in modern chemistry, presenting promising opportunities for sustainable chemical processes and environmental remediation [1–6]. The versatility of this approach stems from its capability to exploit light for inducing chemical reactions using solid-state catalysts. These materials not only display enhanced photostability, but also contain lower quantities of transition metals when compared to their homogeneous (organometallic) counterparts [7,8]. The use of packed beds for the implementation of solid-state catalysts within industrial reactors has been widely documented [9]. This choice is motivated by the capability of packed beds to accommodate catalysts in powder form, thus overcoming the challenges associated to the use of finely dispersed catalytic material commonly employed in slurry reactors – including separation and recovery from the reaction mixture –, while simultaneously reducing the possibility of pressure drops within the system [10–12]. These characteristic of packed bed reactors collectively contribute to enhanced performance and improved operational stability. However, when considering heterogeneous photocatalysts, the utilization of packed bed reactors introduces a distinctive challenge due to limitations in energy transfer. In fact, the introduction of powdered catalysts within

* Corresponding author.
E-mail address: gianvito.vile@polimi.it (G. Vilé).

https://doi.org/10.1016/j.cej.2024.155885
Received 27 May 2024; Received in revised form 13 August 2024; Accepted 15 September 2024
Available online 17 September 2024

packed beds can hinder the propagation of light and energy throughout the reactor's body, potentially compromising the overall efficiency of photocatalytic processes [13,14]. Some of the approaches that have been adopted to address this challenge are schematically illustrated in Scheme 1. For instance, the deposition of catalytic material on micromixer frameworks, nanofibers, or membranes enhances mass transfer and facilitates a more effective light-catalyst interaction [15,16]. Nevertheless, this approach may result in the detachment of the catalyst layer during prolonged reaction times. Another strategy to increase light transfer efficiency consists in reducing the diameter of packed beds to produce extremely thin reactors [17,18]. Furthermore, the addition of glass beads among catalyst particles may help light diffuse within the internal areas of packed beds, mitigating irradiation limitations [19,20]. Unfortunately, achieving a precise control over the position of these glass beads in the reactor is often challenging and may lead to less predictable processes. Despite their inherent limitations, collectively, these solutions have contributed to advancing photocatalytic performance in the field of heterogeneous catalysis. In this context, the conjugation of a heterogeneous photocatalyst with a polymer through *in situ* copolymerization offers a promising solution to address the challenges mentioned above, eventually paving the way for the development of novel types of packed bed photoreactors and allowing precise tuning of the absorption properties of the photocatalytic material. In particular, bicontinuous interfacial jammed emulsion gels, referred to as bijels, are

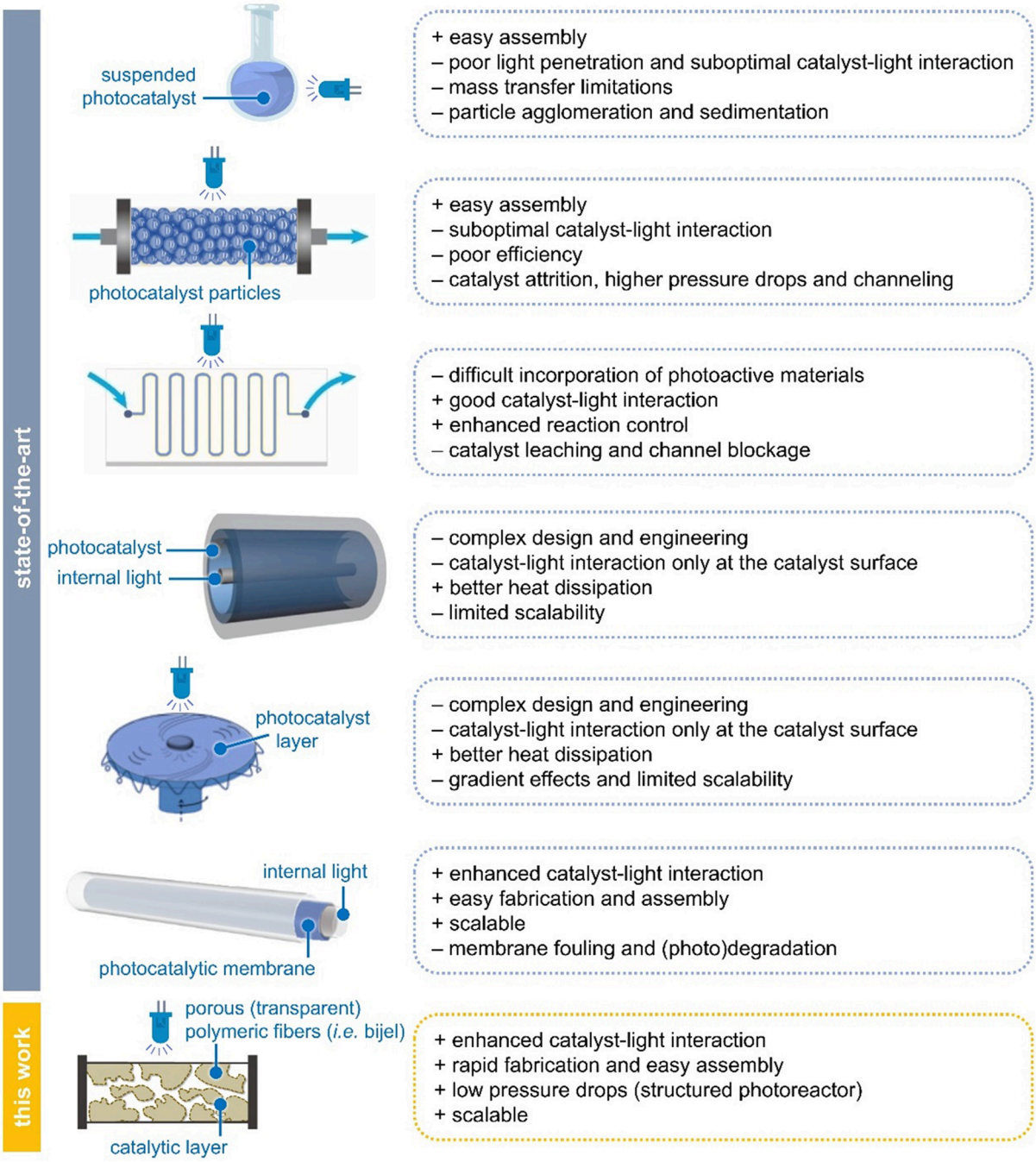

Scheme 1. State-of-the-art reactor designs for heterogeneous photocatalysis. Advances in the design of photoreactors for solid-state heterogeneous catalysis driven by the need to maximize light-catalyst interactions. The development of a novel bijel-based reactor, highlighting its distinctive structure and potential to advance sustainable photochemical processes, is depicted in the final panel.

emerging as transformative materials with broad implications across several chemistry and chemical engineering-related fields such as in separation membranes, drug delivery, and energy-storage technologies [21–23]. These materials exhibit a unique 3D architecture, characterized by the presence of two tortuous, interconnected domains – the catalytic material and a polymer conjugated to the former –, resulting in the formation of a porous bicontinuous structure stabilized by colloidal particles [24,25]. The porous morphology, deriving from the interpenetration of the two material domains, can be finely tailored by controlling nanoparticle size and concentration during synthesis. Although these materials have never been applied in photocatalysis, the incorporation of photoactive particles, including carbon nitride and carbon nitride-supported single-atom catalysts (SACs), in an appropriate polymeric matrix will lead to the development of adjustable catalytic structured matrices suitable for several catalytic processes [26].

In this study, we present an innovative bijel-based photoreactor design obtained through the integration of a polymer, polypentadecalactone (pPDL), and carbon nitride (CN_x). Following the investigation of its structure and physico-chemical properties, we assess the reactor performance in the photodegradation of methylene blue under flow conditions. In addition, the potential and applicability of the reactor system is also demonstrated across diverse photocatalytic reactions, including the photooxidation of benzyl alcohol and photocatalyzed C-N homocoupling of benzylamine. A mathematical model is formulated to describe continuous photocatalytic processes within the newly developed mesophotoreactor, with a specific emphasis on the degradation of the methylene blue dye. Moreover, fluid dynamics simulations underscore the effectiveness of the mesophotoreactor in promoting light diffusion through its channels and improving its interaction with the catalyst, resulting in increased levels of irradiation and enhanced performance compared to traditional packed bed reactors and other systems reported in the literature [27–29]. These advantages, combined with the absence of leaching of catalytic material, minimal pressure drops, and an easy and straightforward design and preparation process, make the mesophotoreactor particularly suitable for future industrial applications.

2. Materials and methods

2.1. Synthesis of the photocatalytic materials

Graphitic carbon nitride (gCN_x) was prepared by thermal polymerization, subjecting cyanamide (10 g; Sigma-Aldrich, 99 %) to a heat treatment at 550 °C for 3 h (heating ramp: 10 °C min^{-1}) [30]. Mesoporous graphitic carbon nitride ($mpgCN_x$) was synthesized employing a hard template-assisted polymerization strategy reported elsewhere [31]. Briefly, cyanamide (3 g; Sigma-Aldrich, 99 %) was added to a suspension of colloidal silica (7.5 g; Sigma-Aldrich, Ludox® HS40) and stirred overnight at 70 °C. The resulting solid was heated at 550 °C for 4.5 h in an alumina crucible (heating ramp: 2.2 °C min^{-1}). The obtained material was then added to a 4.2 M solution of ammonium hydrogen difluoride (NH_4HF_2, 12 g in 50 mL of water; Sigma-Aldrich, 95 %), kept at room temperature for 24 h under stirring, and finally centrifuged and washed with water and ethanol to achieve the final catalyst. The CN_x-supported SACs were synthesized following an already reported preparation strategy [32]. An aqueous solution of inorganic chlorinated metal-containing salt (10 mmol in 10 mL of water; Sigma-Aldrich, 99 %) was mixed with an aqueous solution of sodium tricyanomethanide (10 mmol in 10 mL of water; Sigma-Aldrich, 99 %). Upon stirring at room temperature for 3 h, the resulting mixture was filtered to recover the solid metal tricyanomethanide salt, washed with water, and dried overnight under vacuum conditions. The as-obtained salt (37 mg, 0.015 mmol) was added to a suspension of colloidal silica (7.5 g; Sigma-Aldrich, Ludox® HS40) and stirred overnight at 70 °C. The resulting solid was heated at 550 °C for 4.5 h in an alumina crucible (heating ramp: 2.2 °C min^{-1}). The obtained material was then added to a 4.2 M solution of NH_4HF_2 (12 g in 50 mL of water; Sigma-Aldrich, 95 %), kept at room temperature for 24 h under stirring, and finally centrifuged and washed with water and ethanol to afford the final catalyst. The metal-containing SACs synthesized following the procedure outlined here will be denoted as Mn@$mpgCN_x$, Zn@$mpgCN_x$, and Ni@$mpgCN_x$ throughout this article.

2.2. Preparation of the bijel mesophotoreactor

Triazabicyclodecene (TBD, 0.28 mmol, 0.04 equiv.; Sigma-Aldrich, 99 %) was added to a mixture of ω-pentadecalactone (PDL, 7 mmol, 1 equiv.; Sigma-Aldrich, 99 %) and ethanol (1.4 mmol, 0.2 equiv.; Sigma-Aldrich, 99 %), and the resulting solution was stirred at 80 °C for 1.5 h to reach the desired degree of polymerization. Then, 60 mg of photoactive material was dispersed in 3 mL of deionized water, sonicated at room temperature using an ultrasonic probe (Fisherbrand™ Model 120 Sonic Dismembrator) at 30 W for 15 min, added to the polymeric mixture, and stirred at 90 °C until the formation of a solid porous structure (herein, denoted as "mesophotoreactor"). The obtained mesophotoreactor was dried at 60 °C for 5 h under vacuum, and then employed as such for the catalytic evaluations.

2.3. Materials characterization

The porous nature and surface area of the materials were assessed *via* nitrogen physisorption measurements with a Micromeritics® ASAP™ 2020 instrument. Following an outgassing pre-treatment at 150 °C for 24 h aimed at removing any adsorbed contaminant and residual moisture from the catalytic surfaces, the adsorption/desorption isotherms were collected at −196 °C using nitrogen as the probing gas. The surface area values were determined applying the Brunauer-Emmett-Teller (BET) theory on the adsorption branch of the isotherms considering the $0.05 < p/p_0 < 0.3$ pressure range as this corresponds to the transition from the monolayer to the multilayer of nitrogen gas molecules adsorbed on the materials' surfaces. The chemical composition of the catalysts was investigated by CHNS elemental analysis performed using a Vario Micro Element Analyzer, after their combustion at high temperatures and the quantification of the resulting compounds in the gas form. The Mg, Zn or Ni content loaded on the $mpgCN_x$-supported catalysts was evaluated through inductively coupled plasma optical emission spectroscopy (ICP-OES) using a PerkinElmer® Optima™ 8300 equipment. The materials were dissolved in a strong acidic medium, nebulized, and finally exposed to an inductively coupled plasma torch to generate excited species emitting photons at wavelengths characteristic of specific chemical elements, thus enabling the identification and quantification of the metal loadings. Solid-state cross-polarization/magic angle spinning nuclear magnetic resonance (CP-MAS NMR) spectroscopy was employed to acquire ^{13}C and ^{15}N NMR spectra on a Bruker Neo spectrometer with a superconducting ultra shield magnet of 11.7 T equipped with a commercial 4 mm MAS iProbe. Materials were finely ground, packed in zirconia rotors, and finally introduced in the instrument for the spectroscopic measurements. The following conditions were applied: repetition time 4 s, contact time 8 ms, spin rate 10 kHz. Infrared spectra were collected using a Thermo Scientific Nicolet™ iS20 FTIR spectrometer hosting the corresponding Smart iTX setup for attenuated total reflection-Fourier transform infrared (ATR-FTIR) measurements. 128 interferograms recorded with a resolution of 2 cm^{-1} were typically averaged to yield the final infrared spectra. Scanning electron microscopy (SEM) and energy-dispersive X-ray (EDX) analyses were performed with a Philips XL30 instrument in low vacuum mode (−0.8 torr) equipped with an EDX element probe for elemental mapping. Confocal laser scanning microscopy (CLSM) measurements were performed on a custom-built confocal setup. For the excitation, 405/488 nm 40 MHz pulsed diode lasers (PDL 800-B driver with LDH-D-C-405/LDH-P-C-485B diodes, PicoQuant) were employed. A quarter-wave-plate was used in the excitation path to convert linear to circular polarisation. The

laser beam was coupled into a single-mode fiber (PMC-460Si-3.0-NA012-3APC-150-P, Schäfter + Kirchhoff) with a fiber-coupler (60SMS-1–4-RGBV-11–47, Schäfter + Kirchhoff). After the fiber, the output beam was collimated by an air objective (UPlanSApo 10×/0.40NA, Olympus). After passing through a clean-up filter (MaxDiode 405/10, Semrock or ZET 488/10, Chroma), an ultra-flat quad-band dichroic mirror (ZT405/488/561/640rpc, Chroma) directed the excitation light toward the microscope. The excitation beam was directed into a laser scanning system (FLIMbee, PicoQuant) and then into a custom side port of the microscope (IX73, Olympus). The three galvo-mirrors in the scanning system were capable of deflecting the beam while preserving its position in the backfocal plane of the objective (UPIanSApo 60×, Olympus). The sample position was adjusted thanks to manual *xy* stage (Olympus) and a *z*-piezo stage (Nano-ZL100, MadCityLabs). Emission fluorescence light was collected by the same objective and de-scanned in the scanning system. Afterwards, an achromatic lens (TTL180-A, Thorlabs) was used to focus the beam onto the pinhole (100 μm P100S, Thorlabs). The excitation laser light was blocked in the emission path by a band-pass filter (BrightLine HC 460/60, Semrock) or by a long-pass filter (561 LP Edge Basic, Semrock). The emission light was collimated by a 100 mm lens, and then focused on a SPAD-detector (SPCM-AQRH, Excelitas) with an achromatic lens (AC254-030-A-ML, Thorlabs). The output signal of the photon detector was recorded by a time-correlated single photon counting (TCSPC) system (HydraHarp 400, PicoQuant) synchronized with the triggering signal from the excitation laser. Typically, sample scans were acquired with a virtual pixel size of 100 nm, a dwell time of 2.5 μs/pixel, and a TCSPC time resolution of 16 ps. To investigate the internal structure of the bijel reactor, we turned to CLSM. The labelling procedure with Nile Red dye was carried out according to the following protocol. First, a small portion of bijel-based reactor was cut with a sharp scalpel and immersed in a 1 μM solution of Nile Red (in distilled water) for 30 min. Then, the material was washed with distilled water, transferred to the microscope and placed between two coverslips in the water medium. The tridimensional cross section of bijel-based reactor was elucidated *via* computed tomography (CT) performed using an industrial microCT system (BIR Actis 130/150, upgraded). The scanning plane was horizontal and perpendicular to the axis of the cylindrical reactor body. Based on geometry and dimensions of the material, a cubic voxel of 0.012 mm was obtained. Segmentation and binarization of 2D slices from microCT technique were carried out by means of Avizo™ (Mercury) software to detect pores. The thermal stability of the synthesized mesophotoreactor was evaluated by thermogravimetic analysis (TGA) using a PerkinElmer® STA 6000 analyzer. For each analysis, samples were heated from 30 to 900 °C at a heating rate of 10 °C min^{-1}. ^{1}H HR-MAS NMR were performed on a Bruker NEO spectrometer operating at 500 MHz proton frequency, equipped with a dual $^{1}H/^{13}C$ high-resolution magic angle spinning (HR-MAS) probe head. The samples were transferred in zirconia rotors with a volume of 12 μL. All data were acquired at 305 K with a spinning rate of 4 kHz. The diffusion measurements were performed employing diffusion ordered spectroscopy (DOSY) methods with a bipolar pulse longitudinal eddy current delay (BPPLED) pulse sequence [33]. The duration of the magnetic-field pulse gradients (δ) and the diffusion times (t_d) were optimized for each sample to obtain complete dephasing of the signals with the maximum gradient strength. For the investigated samples, t_d = 20 ms and δ = 3 ms. The pulse gradients were increased linearly from 2 to 95 % of the maximum gradient strength. In each experiment, a series of 32 spectra with 32,000 points was collected with a relaxation delay of 10 s. The diffusivity studies (DOSY experiments) were replicated three times to validate the results.

2.4. Photocatalytic experiments

All reactants and solvents used for the photocatalytic experiments were purchased by Sigma-Aldrich and used as such without any further purification. To validate the formation of products in selected photoreactions, various characterization techniques were employed. UV–Vis absorption spectroscopy was conducted using a Thermo Scientific GENESYS™ 140/150 Vis/UV–Vis spectrophotometer, with detection focused at 664 nm. High-performance liquid chromatography (HPLC) measurements were conducted with the Agilent™ 1260 Infinity II LC System, equipped with a variable wavelength detector G7114A tuned at λ = 210 nm, and a C_{18} HypersilGOLD 5 μm 175 Å column (Thermo-Fisher). Samples were analysed using a mobile phase composed of MeCN/H_2O in a 60 %/40 % ratio and a total flow rate of 0.7 mL min^{-1}. ^{1}H and ^{13}C NMR spectra were recorded on a Bruker Avance 400 MHz spectrometer, and chemical shifts were reported in parts per million (ppm) downfield from tetramethylsilane.

The bijel mesophotoreactor (500 mg in weight, containing ~20 mg of photoactive CN_x material) was prepared following the procedure reported in Section 2. At the end of the synthesis, with the material still in the liquid form, it was transferred in a transparent fluorinated ethylene-propylene (FEP) tube (25 cm long, 3.2 mm o.d., and 2.1 mm i.d.). After the catalytic material cooled and solidified, quartz wool was inserted into the FEP tube. The reactor volume was calculated dividing the difference in mass between the dry photoreactor and reactor filled with the reaction solvent by the solvent density. The reaction mixture was pumped into the reactor using a syringe pump (Harvard PHD ULTRA™), equipped with a 25 mL gastight syringe (Hamilton™), and irradiated at different light wavelengths (128 W) using a commercial PhotoCube™ (ThalesNano) apparatus. The experimental setup described here is illustrated in Figure S1.

The potential and applicability of the bijel-based reactor systems were evaluated across diverse photocatalytic reactions. For the photodegradation of methylene blue (MB), MB was dissolved in deionized water to reach the desired final concentration. 20 mL of the resulting solution were pumped into the mesophotoreactor under 457 nm LED irradiation at 40 °C, testing different flow rates. 2 mL of solution were collected and analysed by UV–Vis absorption spectroscopy. Regarding the photooxidation of benzyl alcohol (BnOH), BnOH (0.19 mmol) was dissolved in deionized water (5 mL) and pumped in the mesophotoreactor under 457 nm LED irradiation at 40 °C, using a flow rate of 0.006 mL min^{-1}. 0.3 mL of solution were withdrawn, diluted with 1.5 mL of pure acetonitrile, and analysed by HPLC. For the photocatalytic amination, 4-bromobenzonitrile (0.16 mmol, 1 equiv.) was added to a solution of H_2O/EtOH in a 1:1 ratio (2 mL) containing sodium azide (0.8 mmol, 5 equiv.) and triethylamine (0.32 mmol, 2 equiv.). The reaction solution was purged with nitrogen gas for 10 min and pumped into the tubular system under white-LED irradiation at 33 °C, utilizing a flow rate of 0.003 mL min^{-1}. The collected solution was diluted with water (3 mL) and extracted with ethyl acetate (5 mL). The combined organic layers were dried over sodium sulfate, filtrated, and concentrated under vacuum. ^{1}H and ^{13}C NMR spectroscopy measurements were performed to characterize the final product. Finally, the performance of the bijel-based reactor was evaluated in the photocatalyzed C-N homocoupling: benzylamine (0.08 mmol) was dissolved in a mixture of MeCN/H_2O in a 1:1 ratio (2 mL). The reaction solution was pumped into the photocatalytic reactor under 457 nm LED irradiation at 40 °C, using a flow rate of 0.003 mL min^{-1}. The collected solution was diluted with water (3 mL) and extracted with ethyl acetate (5 mL). The combined organic layers were dried over sodium sulfate, filtrated, and concentrated under vacuum. The generation and quantification of the final product were determined by ^{1}H and ^{13}C NMR spectroscopy measurements.

2.5. Computational details

The description of the MB photodegradation process in the tubular mesophotoreactor was based on the development of macroscopic model equations in cylindrical coordinates, including the flow of the reaction solution through the mesoporous material, the scattering of light by the material through the transparent wall leading to a dynamic change in the kinetic rate constant of the photocatalytic reaction across the cross-

section, and the convective-diffusive transport through the mesophotoreactor. The model equations, along with their corresponding boundary conditions, were numerically solved using the implicit finite difference method. The algorithm, containing code to minimize the sum of squared deviations between predicted and experimental data, was developed using *Mathematica* programming language. Validation of the model equations through numerical analysis and simulations under various process and operating conditions were performed using the *Wolfram Mathematica* (Version14.0) software package [34].

Moreover, computational simulations related to the radiation diffusion through the bijel reactor in comparison with an equivalent mesophotoreactor containing a catalytic packed bed were carried out by means of the Ansys Fluent 19.1 suite of programs. Among the various methods available to solve the radiant transfer equation (RTE), the discrete ordinate model was selected due to its enhanced accuracy [35]. This method solves the RTE dividing it by a finite number of discrete solid angles, each associated with a vector direction fixed in the global Cartesian system ($\vec{x}, \vec{y}, \vec{z}$). To avoid undesired phenomena such as the Ray effect and angle overhanging, a sufficiently high value of angular discretization and pixelization must be chosen [36]. Based on previous works, it was found that values of angular discretization equal to 8×8 and pixelization equal to 3×3 were sufficient to ensure reliable results [37].

3. Results and discussion

3.1. Synthesis and characterization of the bijel mesophotoreactor

Metal-free gCN_x, $mpgCN_x$, and metal-containing SACs ($Mn@mpgCN_x$, $Zn@mpgCN_x$, and $Ni@mpgCN_x$) were synthesized as detailed in Section 2. The chemical compositions, metal contents, surface areas, and pore volumes of the catalysts are reported in Table S1 and are in agreement with experimental data of previous studies related to CN_x-supported SACs [30,38–40]. The powdered photocatalysts were

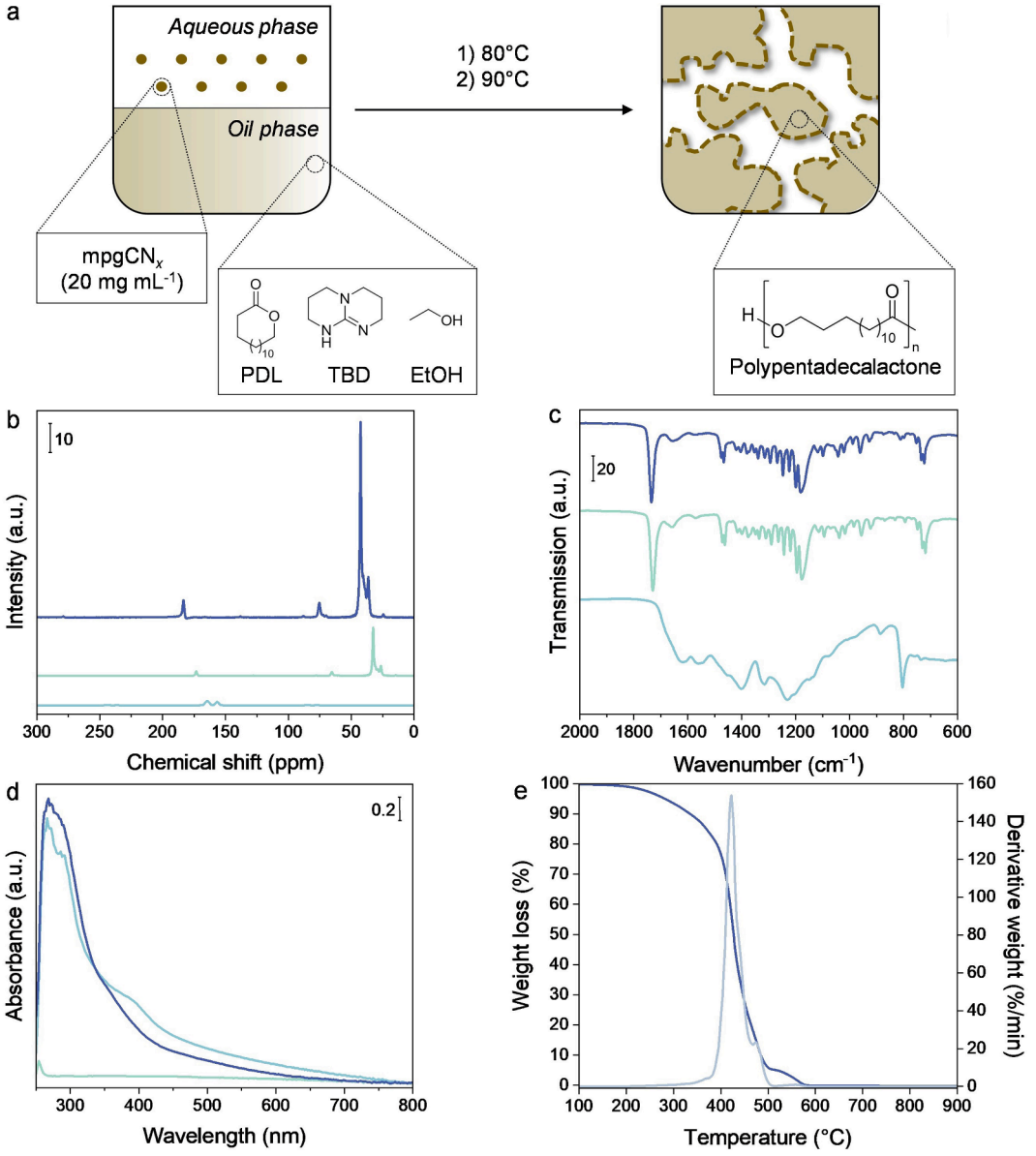

Fig. 1. Integrated materials analysis of a mesophotoreactor confining $mpgCN_x$ and reference powdered materials. Schematic representation of the mesophotoreactor preparation process (a). ^{13}C CP-MAS NMR (b), ATR-FTIR (c), and UV–Vis absorption (d) spectra of $mpgCN_x$ (light blue), pPDL (teal), and of the powdered material deriving from the mesophotoreactor confining $mpgCN_x$ (dark blue). TGA data (dark blue) and the corresponding first derivative curve (grey) of the powdered material deriving from the mesophotoreactor confining $mpgCN_x$ (e).

used as starting materials for preparing the corresponding bijel mesophotoreactors. Briefly, PDL was subjected to thermal-induced ring-opening polymerization, ultimately leading to the production of the polypentadecalactone (pPDL) polymer as the hydrophobic phase of a Pickering emulsion. The aqueous phase was obtained by suspending the CN_x-based powders in water, with a 1:1 vol ratio compared to the polymer. The combination of aqueous and non-aqueous phases, resulting from the entrapment of water in the polymeric network, in the absence of coalescence phenomena, led to the formation of a bicontinuous architecture schematically depicted in Fig. 1a. Several factors are known to affect the final structure of bijel-based materials [41–43], including the particle size and concentration of the CN_x phase. The average particle size of CN_x, as determined by dynamic light scattering (DLS), was found to lie at *ca.* 150 nm. Additionally, various concentrations of the CN_x phase were tested: an increase in its concentration resulted in unstable bicontinuous architectures, while a reduction in its concentration compromised the photocatalytic activity of the composite material. Thus, a trade-off between preserving the structural integrity of the bicontinuous system and ensuring an adequate CN_x concentration for effective photocatalysis was found (see Section 2). A series of bijel mesophotoreactors, incorporating the catalytic powders mentioned earlier, were prepared and characterized, and their performance was evaluated in reactions of interest. However, to streamline the discussion of the results, the reactor confining $mpgCN_x$ was selected as a representative example and subjected to more advanced characterizations and experimental evaluations.

The $mpgCN_x$-based mesophotoreactor, the powdered $mpgCN_x$, and the pPDL polymer were characterized by solid-state CP-MAS NMR spectroscopy (Fig. 1b). The ^{13}C CP-MAS NMR spectrum of $mpgCN_x$ displayed two sharp signals localized at 156.7 and 164.5 ppm which were assigned to the presence of carbon atoms interacting with three aromatic nitrogen atoms, and to carbons simultaneously bonded to two aromatic nitrogens and a defective amine site, respectively [44]. The ^{13}C CP-MAS NMR spectrum of the lactone polymer featured a plethora of signals localized in three main regions, and ascribable to the presence of methylene groups (20 and 40 ppm), α-methoxy carbons (60 and 70 ppm), and carbonyl moieties (169 and 177 ppm) [45]. Finally, the solid-state ^{13}C CP-MAS NMR spectrum of the powdered material resulting from the grinding of the mesophotoreactor incorporating $mpgCN_x$ showed characteristic signals of both the polymer and the photocatalyst, thus confirming the successful integration of both components in the bijel reactor. An enlarged view of the of the 140–180 ppm region in the ^{13}C CP-MAS NMR spectrum of the mesophotoreactor confining $mpgCN_x$ has been included in Figure S2 to properly display the two signals localized at 156.7 and 164.5 ppm arising from the presence of CN_x within the reactor. The diminished intensity of these signals was attributed to the predominant presence of the polymeric phase within the mesophotoreactor composition, relative to that of carbon nitride. Infrared spectra of $mpgCN_x$, pPDL, and the functionalized mesophotoreactor biphasic porous structure are shown in Fig. 1c. The $mpgCN_x$ spectrum showed a broad absorption band between 1700 and 1150 cm^{-1}, corresponding to the vibrational stretching modes of the aromatic rings composing the CN_x structure, and a sharp characteristic band at 810 cm^{-1}, attributed to the breathing mode of the heteroaromatic units [46,47]. ATR-FTIR spectra of pPDL and the functionalized mesophotoreactor featured an additional sharp signal at 1730 cm^{-1}, which was assigned to C═O stretching modes of ester groups present in the lactone polymer structure [48]. The spectral region localized between 1250 and 1100 cm^{-1} contained contributions arising from symmetric and asymmetric C—O—C stretching vibrations [48]. Even if most of the infrared signals characteristic of CN_x could not be observed in the spectrum of the bijel reactor composite material, the presence of the band at 810 cm^{-1} in the spectra of both $mpgCN_x$ and bijel composite highlighted the successful incorporation of the powdered photocatalyst into the reactor body. The UV–Vis absorption spectra of $mpgCN_x$, pPDL, and the powdered material derived from the $mpgCN_x$-containing mesophotoreactor are shown in Fig. 1d. The comparable absorption profile of $mpgCN_x$ and composite bijel material demonstrated the efficient incorporation of the former in the biphasic porous structure, with retention of its photon absorption capacity. On the other hand, pPDL was found to lack the ability to absorb photons beyond 200 nm, indicating its potential inertness in any photocatalytic process. TGA analysis on the $mpgCN_x$-confining reactor material was performed to assess its thermal stability, and therefore its possible application in photochemical processes carried out at medium/high temperatures. Fig. 1e depicts the TGA curve related to the mesophotoreactor composite material recorded from 100 ℃ to 900 ℃ at 10 °C min^{-1}. Here, the polymer underwent irreversible pyrolysis between 350 and 550 °C, resulting from the single-step thermal degradation of the C—O—C groups present in the pPDL polymer composing one of the domains of the mesophotoreactor [49]. Nevertheless, the relatively high thermal stability of the structured reactor body up to 200–250 °C ensure long-term stability of the composite matrix for many fine chemical processes, and even during prolonged low-temperature light irradiation.

Representative SEM images of the porous architecture of the bijel-based mesophotoreactor and the corresponding elemental EDX map are shown in Fig. 2b and c. The presence of spherical structured aggregates with a diameter of ~10 μm (Fig. 2b, inset) was attributed to the $mpgCN_x$ phase, in line with the CLSM observations (*vide infra*). The EDX elemental mapping confirmed the incorporation of carbon nitride in the polymeric matrix and its homogeneous distribution within the reactor structure. To investigate the internal conformation of the bijel reactor, the pPDL polymer was labelled with Nile Red (for the detailed procedure, refer to the Supplementary Material), a widely employed dye for visualizing polymeric structures due to its peculiar photophysical and spectroscopic properties [21,39]. More specifically, it is nearly nonfluorescent in water and other polar environments but exhibits enhanced fluorescence when interacting with hydrophobic compounds or apolar portion of polymers. We observed and confirmed the fiber-like, polymeric porous morphology of the mesophotoreactor, and the presence of $mpgCN_x$ aggregates because the emission band of the latter was significantly blue shifted compared to that of Nile Red (Fig. 2d). By exploiting a 405 nm excitation wavelength, we selectively imaged $mpgCN_x$ nanoparticles while the polymer matrix remained unobserved. To validate our findings, we conducted additional CLSM experiments as controls, capturing images of both unlabeled $mpgCN_x$-doped material and the pure pPDL polymer. The internal morphology of the material was also investigated through microCT, as shown in Fig. 2e and f. The spherical shape and the homogeneous distribution of the pores, with a modal diameter of 0.20 mm, featured the whole volume of the prepared material, with an average pore diameter of 527.0 Å determined by porosimetry tests. The pores were mainly concentrated along a central vertical axis originating from a larger pore and presenting three branches pointing to the outer edge of the specimen with an angle of ~120° (Fig. 2f). Rounded vesicles with sizes comparable to that of the pores and filled by a denser material (light grey, Fig. 2e) were observed throughout the sample. Also, the presence of some isolated pores at the border of the reactor body was detected during the microCT analysis. The 3D reconstruction enabled by this technique provided a complete microstructural representation of the main features of the bijel-based reactor configuration, including tight distributions of domain sizes, high connectivity between channels, and an overall tortuosity of the reactor structure.

Given the high degree of porosity of the bijel reactor's structure, we attempted to measure the diffusivity of potential reactive molecules passing through the mesophotoreactor. In particular, in order to measure the molecular diffusion motion over a known observation time (t_d), ^1H HR-MAS NMR spectra of the mesophotoreactor material were recorded resorting to the DOSY NMR technique with pulse field gradients (PFG) of increasing intensity along a defined axis (usually, *z*-axis). A conventional analysis of the 2D experiment yielded a 2D map encoding for each observed species, with the chemical shift (δ) reported on the horizontal axis and their diffusion coefficient (D) in the vertical

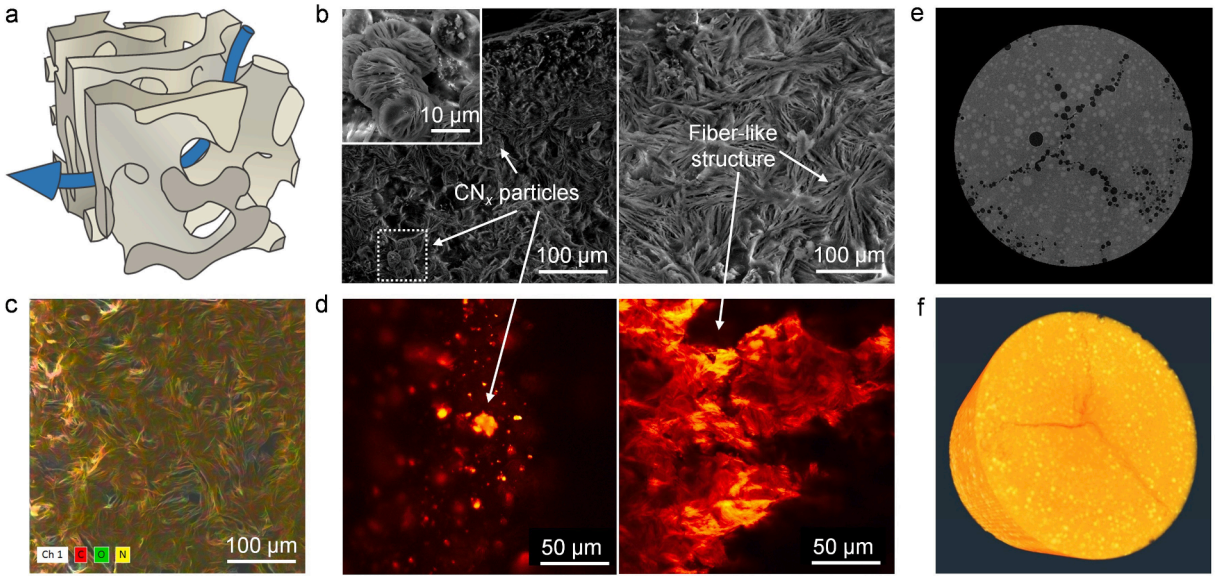

Fig. 2. Advanced visual inspection of the mesophotoreactor confining mpgCN$_x$. 3D representation of the bijel-based reactor structure, showcasing the porous nature of the composite material (a). SEM image capturing the cross-sectional view of the sample (b), along with the corresponding EDX maps of carbon, oxygen, and nitrogen species (c). CLSM image and Nile Red labelling revealing mpgCN$_x$ confined within the microreactor porous structure (d). Front view of the bijel-based mesophotoreactor by microCT (e), where darker areas represent the free volume available for the catalysis, and 3D reconstruction of the whole mesophotoreactor predicted via tomographic technique (f).

dimension [50]. Fig. 3a shows the ^{1}H DOSY map that confirmed the bicontinuous structure of the material featuring two separate domains – water and an organic compound (polycaprolactone, PCL) – annotated in the map. Following a different processing of the experimental data, the molecular mean square displacement $\langle z^2(t_d)\rangle$ could be calculated by fitting the gradient dependent signal intensities $I(q,t_d)$ according to the following Eq. (1):

$$I(q,t_d) = I_0 \exp\left(-\frac{1}{2}q^2\langle z^2(t_d)\rangle\right) \quad (1)$$

where $q = \frac{\gamma g \delta}{2\pi}$, and in particular γ is the gyromagnetic ratio of the observed nucleus, δ is the gradient pulse duration, and g is the intensity. For isotropic solutions, the mean square displacement scales linearly with the observation time t_d according to Eq. (2):

$$\langle z^2(t_d)\rangle = 2Dt_d \quad (2)$$

where D is the diffusion coefficient. The normalized experimental signal decays ($I(q,t_d)/I(0,t_d)$) versus the gradient pulse amplitude is reported in Fig. 3b and c. The diffusion coefficient within the bijel structure was D=4.4 × 10^{-10} m^2 s^{-1}, a lower value than the bulk water solution D_0 = 2.7 × 10^{-9} m^2 s^{-1}, indicating the presence of tortuous interconnected domains typical of bijels. Indeed, the diffusivity of D_2O samples is consistent with the value of free diffusion present in literature, underlining the absence of diffusion barriers or obstacles [51]. This is typical of bicontinuous structures, different from the condition of emulsions. The ratio of D over D_0 ($\tau = 0.16$) reflected the tortuosity of the diffusion motion through the mesophotoreactor structure.

3.2. Catalytic performance of the bijel mesophotoreactor

The photocatalytic activity of mesophotoreactors confining gCN$_x$, mpgCN$_x$, Ni-, Zn- or Mn-containing SACs was evaluated in several light-driven reactions of interest under flow conditions. The bijel composite material was packed in a transparent FEP tube (see Section 2) and tested in the blue light-activated MB photodegradation. The selected model reaction was performed using a 44 μM aqueous solution of the dye, based on preliminary concentration tests and control experiments reported in Tables S2 and S3. In the absence of catalyst, no MB degradation occurred. Only when the chemical process was carried out in the presence of mpgCN$_x$ and under blue light irradiation, the MB photodegradation was observed. To optimize the reaction conditions in a

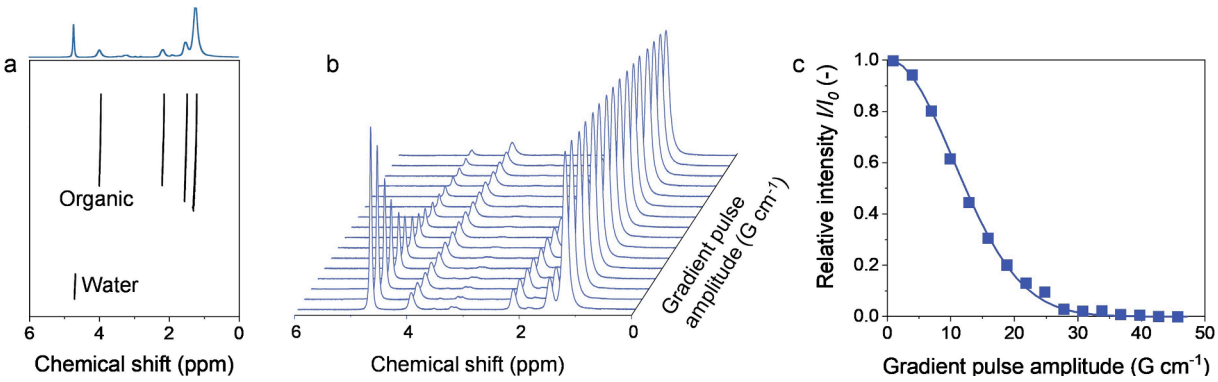

Fig. 3. Diffusivity in the mesophotoreactor structure. Mapping of the mesophotoreactor composite material through ^{1}H HR-MAS NMR and DOSY experiments (a), with the decay of the NMR signal intensity versus the gradient pulse amplitude reported in (b) and (c).

continuous-flow mode, MB degradation was tested at different residence times (τ), as exemplified in Fig. 4a. Between 5 and 15 min, a *quasi*-linear increase of the process efficiency was observed, followed by some sort of plateau, with a final degradation of MB of 99 % achieved with a 60-min residence time. Fig. 4b presents the comparative catalytic results related to bijel photoreactors confining metal-free CN_x or metal-containing SACs with a 5-minute residence time to display the differences between the screened photocatalytic systems. The two metal-free photocatalysts, namely gCN_x and $mpgCN_x$, exhibited similar activity in the photocatalytic degradation of the MB dye. In contrast, the use of metal-containing $mpgCN_x$ in the reactor led to increased degradation rates, with no relevant differences due to the metal element loaded on the CN_x support material (*i.e.*, Mn, Zn, and Ni). The stability of the prepared photocatalytic systems was assessed by conducting the continuous-flow reaction over three consecutive cycles. Excellent photostability and recyclability of the produced biphasic porous structure and no activity losses were observed when $mpgCN_x$-based materials were employed (Fig. 4c). In contrast, the use of the gCN_x led to a decrease in the MB degradation rate due to the partial deactivation of the photocatalytic material. Leaching experiments revealed no evidence of loss of photocatalytic material from the reactor systems. Moreover, the structured mesophotoreactors demonstrated stable activity across three reaction cycles of MB photodegradation, as shown in Fig. 4c. This consistent performance suggested that catalyst leaching from the reactor system did not occur, as leaching would typically result in a considerable decrease in the mesophotoreactor activity over time. Additional details on catalytic experiments and analyses are provided in the Supplementary Material. This includes the impact of residence time (1–30 min) on MB photodegradation (Figure S3), a comparative kinetic study of MB degradation under batch and flow conditions (Figure S4), the influence of MB concentration on degradation efficiency using a mesophotoreactor integrating $mpgCN_x$ under flow conditions (Table S3), and a chemical oxygen demand (COD) analysis conducted during MB photodegradation in the same mesophotoreactor setup (Table S4).

The scope of this work was finally expanded to include additional industrially relevant synthetic processes, with the purpose of proving multiple potential applications of the novel bijel photocatalytic reactor system. The reactions were carried out without optimizing the operating conditions, solely to demonstrate the broad applicability of the bijel reactor. Notably, its porous structure containing nickel single atoms supported on $mpgCN_x$ provided the desired products in good yields in all the reactions of interest. The photooxidation of benzyl alcohol led to the formation of the desired benzaldehyde with a 27 % yield after 1 h, using air as oxidizing agent and water as solvent (Scheme 2a). The photocatalytic amination of *p*-bromobenzonitrile was performed in presence of sodium azide (NaN_3) and triethylamine (Et_3N) under white light irradiation, leading to the generation of the corresponding *p*-aminobenzonitrile (24 %) (Scheme 2b). A 30 % yield of product was achieved when the bijel mesophotoreactor was employed in the C-N homocoupling reaction of benzylamine (Scheme 2c).

3.3. Model development

The development of a mathematical model to describe continuous photocatalytic processes in a tubular mesophotoreactor relied on the assumption of a consistently uniform structure within a porous bijel-based architecture, encapsulating CN_x materials homogenously dispersed across the reactor body. In a steady-state process, the governing momentum balance equation could be represented by a Brinkman equation [52]:

$$\begin{cases} \nabla P = -\frac{\mu}{\kappa}\vec{v} + \nabla \bullet \mu_e\left(\nabla\vec{v} + \nabla\vec{v}^{T}\right) \\ \nabla \bullet \vec{v} = 0 \end{cases} \quad (3)$$

where $\nabla \bullet \vec{v} = 0$ is a continuity equation, P is the fluid pressure, $\vec{v}$ is the fluid superficial velocity, μ is the fluid viscosity, μ_e is the so-called effective viscosity of the fluid in the porous media, and κ is the permeability tensor.

For a laminar, stationary, isothermal, unidirectional flow of a Newtonian fluid, considering an axisymmetric cylindrical system (Fig. 5b), with the additional assumption of the pressure gradient along the *x*-direction being constant and equal to $-\Delta p/L$ (Pa m^{-1}), where L is the length of the tubular reactor, Eq. (3) reduces to:

$$0 = -\frac{\Delta p}{L} - \frac{\mu}{\kappa}v_x + \mu_e\frac{1}{r}\frac{\partial}{\partial r}\left(r\frac{\partial v_x}{\partial r}\right) \quad (4)$$

In Eq. (4), μ/κ represents the reciprocal of the permeability – which takes into account the flow resistance of the porous medium –, where μ is

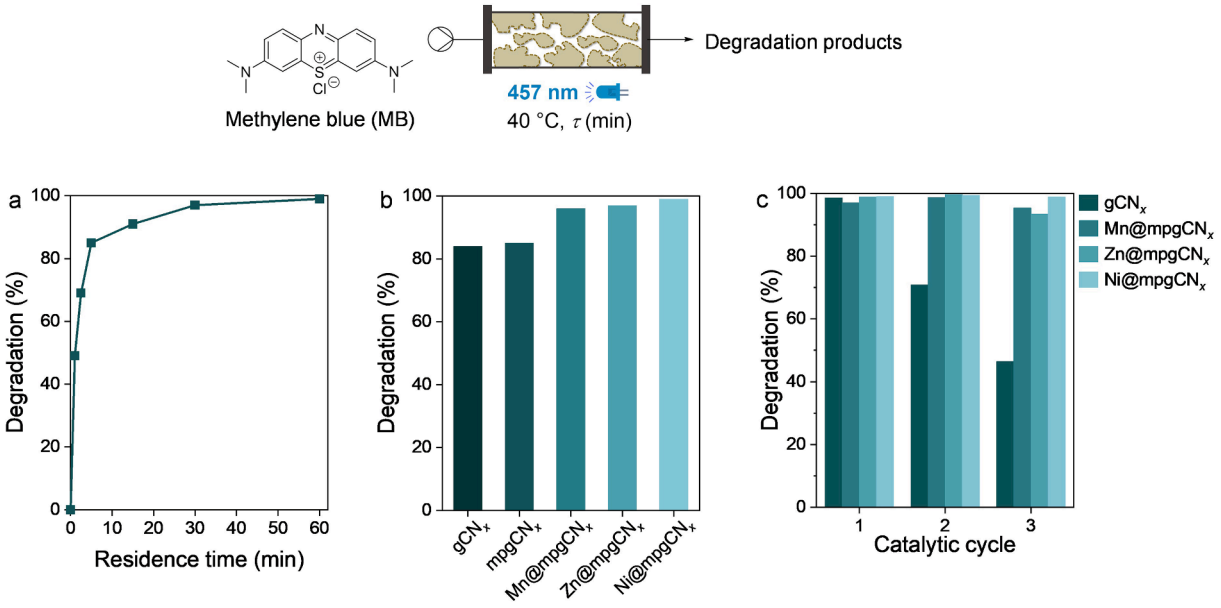

Fig. 4. Photocatalytic degradation of MB. Effect of residence time on the MB degradation rate using a mesophotoreactor confining $mpgCN_x$ (a). Evaluation of the photocatalytic activity of mesophotoreactors confining gCN_x, $mpgCN_x$ or metal-containing SACs (b). Evaluation of the mesophotoreactor stability over three reaction cycles (c). Reaction conditions: MB concentration = 44 μM, λ = 457 nm, T=40 °C, solvent = water.

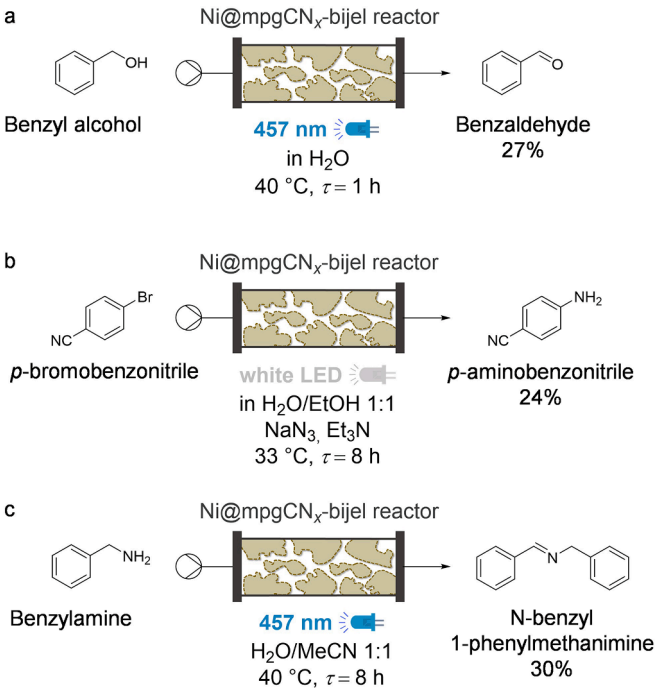

Scheme 2. Photocatalytic scope. Photooxidation of benzyl alcohol (a), photocatalytic amination of *p*-bromobenzonitrile (b), and photocatalyzed C-N homocoupling (c) over a mesophotoreactor confining Ni@mpgCN$_x$.

the dynamic viscosity (Pa s) and κ is the permeability (m^2). v_x is the velocity component in the *x*-direction (m s^{-1}), and *r* is the radial distance from the center of the reactor to its walls (m). It is often assumed that the effective viscosity μ_e can be approximated by the dynamic viscosity of a fluid, $\mu_e = \mu/\epsilon$, which explicitly includes the void space in the Brinkman equation. The use of a bijel-based mesoporous material, characterized by an experimentally estimated average porosity of $\epsilon = 0.6$, allowed for a realistic prediction of the velocity profiles by applying the Brinkman equation in cylindrical coordinates. In a randomly packed porous medium, the permeability tensor κ (m^2) is often treated as a scalar; thus, a constant and homogeneous value for the permeability was assumed throughout the structure of the porous medium. For our bijel-based porous medium, an approximated value for the permeability was obtained by comparing the real flow rates for given pressure drops in the mesoporous catalytic reactor with the flow rates calculated from the Brinkman velocity profiles (Eq. (4)). The estimated constant value for the permeability, $\kappa = 7.5 \times 10^{-3}$ m^2, was used in further model predictions for the concentration profiles in the photocatalytic mesophotoreactor.

The mass balance equation for MB in the symmetric physical domain of the tubular mesophotoreactor (Fig. 5b) led to a mathematical 2D model that describes the convective-diffusive mass transport in the aqueous phase and the kinetics of the photocatalytic degradation of the dye. The model equations for the steady-state operating conditions and the unidirectional laminar flow of an isothermal Newtonian fluid through a bijel-based mesoporous material have the following 2D form (Eq. (5)):

$$0 = -v_x(r)\frac{\partial C_{MB}}{\partial x} + D_{MB}\left(\frac{1}{r}\frac{\partial C_{MB}}{\partial r} + \frac{\partial^2 C_{MB}}{\partial r^2}\right) - k(r)C_{MB} \tag{5}$$

with appropriate boundary conditions (Eq. (6)):

$$\begin{cases} C_{MB}(r,0) = C_{MB,in}; & 0 \le r \le R \\ \dfrac{\partial C_{MB}}{\partial r}\begin{pmatrix} R \\ 0 \end{pmatrix}, x = 0; & 0 \le x \le L \end{cases} \tag{6}$$

where C_{MB}, (mol m^{-3}) is the concentration of methylene blue in the liquid phase, and the $C_{MB,in}$ is the inlet concentration of MB; D_{MB} (m^2 s^{-1}) is the diffusion coefficient of substrate within the bijel-based structure (4.4×10^{-10} m^2 s^{-1}); *L* (m) is the length, and *R* (m) is the radius of the mesophotoreactor; $v_x(r)$ represents the parabolic Brinkmann velocity profile through the mesoporous structure (m s^{-1}); $k(r)$ is the photocatalytic reaction rate constant and depends on the light intensity over the cross-section of the porous structure, and thus on the radius (s^{-1}).

The reaction rate in photocatalysis is influenced by factors such as the concentration of the reactants, the temperature, and the properties of the photons. The number of photons that hit the catalyst surface per unit of time and their energy play a decisive role. The reaction rate constant *k* (s^{-1}) can therefore be made significantly dependent on the light intensity *I* (W m^{-2}) and wavelength λ (nm) and is formulated as follows [53,54]:

$$k = \alpha I = \alpha I_0 e^{-\omega(R-r)} \tag{7}$$

In Eq. (7), the light intensity decreases along the irradiation direction *r* towards the center of the tubular mesophotoreactor and can be reflected using the Lambert-Beer law, $I = I_0 e^{-\omega(R-r)}$ where I_0 is the incident light intensity (W/m^{-2}), and ω is the extinction coefficient (m^{-1}). The latter is known as the effective attenuation coefficient, includes the absorption and scattering effects, and describes how a material attenuates light as it passes through it. Finally, α is constant in units (m^2/s W^{-1}) to be determined from experimental data. The results of the simulations regarding the radiation field inside the structure of the bijel mesophotoreactor are shown in Figure S5, which compares its light distribution with that of a packed-bed of catalyst particles with a 100–300 μm average diameter. In these conditions, the optical thickness – defined as $(k+\sigma_s)\cdot L_s$, where *k* and σ_s are the absorption and scattering coefficient of the species, respectively, and L_S is the optical path of the reactor – was considered negligible [36]. The results corroborated that the open and porous structure of the mesophotoreactor allows the light to enter the channels and diffuse through them. This ensures higher irradiation in the reactor than conventional systems such as packed bed reactors, in which the layers of catalyst can considerably hinder light penetration [36].

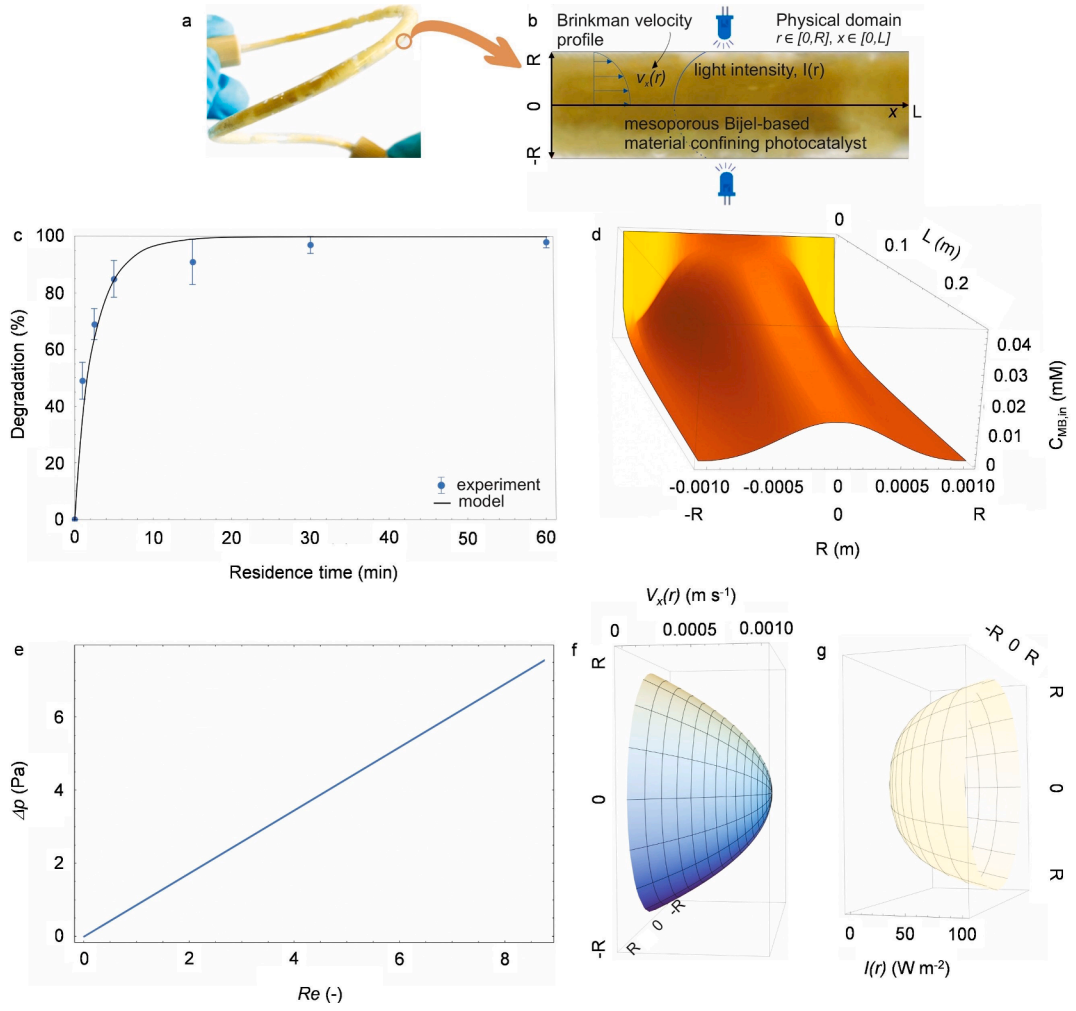

Fig. 5. Modeling of the bijel-based mesophotoreactor. Image of the transparent tubular mesophotoreactor with packed bijel-based material, effectively enclosing the photocatalyst within its porous structure (a). 2D representation of the physical domain of the tubular mesophotoreactor (b). Comparison of model predictions with experimental data of MB degradation (c). The model parameters and constants: internal radius R = 2.1 mm and length L = 250 mm; $C_{MB,in}$ = 44 μM, D_{MB} = 4.4 × 10^{-10} m^2/s, I_0 = 100 W/m^{-2}; α = 0.00037 m/s W^{-1}, ω = 4.2 × 10^{-3} m^{-1}, λ = 457 nm, T=40 °C. Error bars indicate standard deviations of at least triplicates. Concentration profiles of MB (C_{MB}) in the liquid phase along the photocatalytic tubular reactor (d), at a flow rate of 0.1 mL min^{-1} and within a residence time of 5 min. Linear dependence of the pressure drop (Dp) depending on the Reynolds number, Re = $\frac{\rho \bar{v} D}{\mu}$ (/), where $\bar{v}$ is the average velocity (m/s) and D the characteristic dimension of the mesophotoreactor (e). Parametric plot of Brinkman velocity profile (f), at a flow rate of 0.1 mL min^{-1} and within a residence time of 5 min. (f). Parametric plot of light intensity in bijel-based mesoporous material (g) according to Beer-Lambert law with estimated extinction coefficient ω = 4.2 × 10^{-3} m^{-1}.

The 2D model equations for the prediction of the Brinkmann velocity profile in the mesoporous structure and the concentration profiles for the photocatalytic degradation of MB in the mesophotoreactor (Eqs. (3)-(6)) were solved with an implicit numerical finite difference method and using the software tool *Wolfram Mathematica* [34]. The model predictions were numerically verified under different process and operating conditions. In addition to the constant α, the fitting parameter for the system under consideration was the extinction coefficient ω, and based on established least squares minimization methods, we determined the values for $\alpha = 0.00037$ m s^{-1} W^{-1} and $\omega = 4.2 \times 10^{-3}$ m^{-1}. The estimated values were then used to predict MB degradation (%) in a wide range of flow rates and residence times. Based on the successfully performed repeated measurements, we successfully validated our model achieving a good agreement with the measurements without further adjustment of the fitted parameters (Fig. 5c). Fig. 5d shows the concentration profile of methylene blue (C_{MB}) in the liquid phase along the photocatalytic tubular reactor at a flow rate of 0.1 mL min^{-1} and inlet concentration $C_{MB,in} = 44$ μM.

4. Conclusions

In this study, we successfully developed a novel reactor system by confining carbon nitride-supported powdered photocatalysts into a polymeric organic matrix of polypentadecalactone. The structural and physico-chemical properties of the resulting catalytic composite material were assessed through a comprehensive battery of characterization approaches that confirmed the effective incorporation of carbon nitride in the overall structure, the distinctive bicontinuous porous architecture of the latter, and its remarkable stability and applicability in industrial scenarios, exemplified by its performance in the methylene blue photodegradation under flow conditions. Furthermore, the system demonstrated its potential applicability across diverse reactions, including photooxidations and photoaminations. A mathematical model was developed to describe continuous photocatalytic processes in the novel tubular mesophotoreactor, specifically targeting the degradation of the methylene blue dye. The model was successfully validated, showing good agreement with experimental measurements. Fluid dynamics simulations confirmed that the mesophotoreactor's design allows light to penetrate and diffuse through its channels, providing higher

irradiation compared to conventional systems like packed bed reactors. This research opens new avenues for multifunctional catalysis, merging the domains of polymer science and heterogeneous photocatalysis for sustainable chemical transformations.

CRediT authorship contribution statement

Nicolò Allasia: Writing – original draft, Visualization, Investigation, Data curation. **Oleksii Nevskyi:** Investigation. **Marcello Marelli:** Investigation. **Igor Plazl:** Writing – original draft, Investigation, Formal analysis, Data curation. **Jody Albertazzi:** Investigation. **Valentina Busini:** Visualization, Investigation. **Franca Castiglione:** Validation, Investigation. **Filippo Rossi:** Validation, Conceptualization. **Gianvito Vilé:** Writing – review & editing, Writing – original draft, Visualization, Supervision, Project administration, Funding acquisition, Conceptualization.

Declaration of competing interest

The authors declare no known competing financial interests.

Data availability

Data will be made available on request.

Acknowledgements

N.A. acknowledges funding from the European Commission Horizon Europe programme (grant agreement 101057430, SusPharma). O.N. thanks the European Research Council for financial support (grant agreement 884488, smMIET). G.V. acknowledges financial support from Fondazione Cariplo (grant agreement 2022-0713). M.M. thanks Fondazione Cariplo for funding (grant agreement P0000142/2022, e-biochar). I.P. gratefully acknowledges the financial support from the Slovenian Research and Innovation Agency (Grants P2-0191, N2-0342, and L2-3161). Support through M-ERA.NET project BioMat4eye funded by the Ministry of Higher Education, Science, and Innovation of the Republic of Slovenia (Grant No. 9147), and EU Horizon 2020 M.ERA.net (Grant No. 958174) is also acknowledged. The authors are indebted to Prof. Jörg Enderlein and Dr. Alberto Cingolani for useful discussions about confocal laser scanner microscopy and bicontinuous interfacial jammed emulsion gels, respectively. The authors also thank Daniela Dardano and Dr. Alessandra Sivo for the support during synthesis, Dr. Fabio Pizzetti for helping in the production of bijel reactors, Dr. Valeria Vanoli for conducting the DOSY NMR measurements, and Prof. Nicoletta Chiara Fusi for tomography studies.

Appendix A. Supplementary data

Supplementary data to this article can be found online at https://doi.org/10.1016/j.cej.2024.155885.

References

[1] H.L. Tan, F.F. Abdi, Y.H. Ng, Heterogeneous photocatalysts: an overview of classic and modern approaches for optical, electronic, and charge dynamics evaluation, Chem. Soc. Rev. 48 (5) (2019) 1255–1271.
[2] J.C. Colmenares, R. Luque, Heterogeneous photocatalytic nanomaterials: prospects and challenges in selective transformations of biomass-derived compounds, Chem. Soc. Rev. 43 (3) (2014) 765–778.
[3] R. Ciriminna, R. Delisi, Y.-J. Xu, M. Pagliaro, Toward the waste-free synthesis of fine chemicals with visible light, Org. Process Res. Dev. 20 (2) (2016) 403–408.
[4] M. Karimi-Nazarabad, E.K. Goharshadi, M. Aziznezhad, Solar mineralization of hard-degradable amphetamine using TiO_2/RGO nanocomposite, ChemistrySelect 4 (48) (2019) 14175–14183.
[5] R. Mehrkhah, K. Goharshadi, E.K. Goharshadi, H. Sajjadizadeh, Multifunctional photoabsorber for highly efficient interfacial solar steam generation and wastewater treatment, ChemistrySelect 8 (6) (2023) e202204386.
[6] F. Asadi, E.K. Goharshadi, M. Sadeghinia, Highly efficient solar-catalytic degradation of reactive black 5 dye using mesoporous plasmonic Ag/g-C_3N_4 nanocomposites, ChemistrySelect 5 (9) (2020) 2735–2745.
[7] B. Pieber, M. Shalom, M. Antonietti, P.H. Seeberger, K. Gilmore, Continuous heterogeneous photocatalysis in serial micro-batch reactors, Angew. Chem. Int. Ed. 57 (31) (2018) 9976–9979.
[8] X. Wang, S. Blechert, M. Antonietti, Polymeric graphitic carbon nitride for heterogeneous photocatalysis, ACS Catal. 2 (8) (2012) 1596–1606.
[9] K. Lovato, P.S. Fier, K.M. Maloney, The application of modern reactions in large-scale synthesis, Nat. Rev. Chem. 5 (8) (2021) 546–563.
[10] A. Tanimu, S. Jaenicke, K. Alhooshani, Heterogeneous catalysis in continuous flow microreactors: a review of methods and applications, J. Chem. Eng. 327 (2017) 792–821.
[11] G. Kolb, V. Hessel, Micro-structured reactors for gas phase reactions, J. Chem. Eng. 98 (1–2) (2004) 1–38.
[12] M.P. Dudukovic, Frontiers in reactor engineering, Science 325 (5941) (2009) 698–701.
[13] A.P. Udepurkar, K.Y. Nandiwale, K.F. Jensen, S. Kuhn, Heterogeneous photochemical reaction enabled by an ultrasonic microreactor, React. Chem. Eng. 8 (8) (2023) 1930–1936.
[14] H. Zhang, Y. Liu, N. Liu, S. Kang, Understanding the interface properties of photocatalytic reactors for rational engineering applications, J. Chem. Eng. 472 (2023) 145057.
[15] J. Tian, Y. Zhang, L. Du, Y. He, X.-H. Jin, S. Pearce, J.-C. Eloi, R.L. Harniman, D. Alibhai, R. Ye, D.L. Phillips, I. Manners, Tailored self-assembled photocatalytic nanofibres for visible-light-driven hydrogen production, Nat. Chem. 12 (12) (2020) 1150–1156.
[16] Y. Li, D. Zhang, J. Ye, Y. Mai, C. Wang, Y. Yang, Y. Li, F. Besenbacher, H. Niemantsverdriet, F. Rosei, F. Pan, R. Su, A modular tubular flow system with replaceable photocatalyst membranes for scalable coupling and hydrogenation, Ang. Chem. Int. Ed. 62 (22) (2023) e202302979.
[17] A. Chaudhuri, K.P.L. Kuijpers, R.B.J. Hendrix, P. Shivaprasad, J.A. Hacking, E.A. C. Emanuelsson, T. Noël, J. van der Schaaf, Process intensification of a photochemical oxidation reaction using a rotor-stator spinning disk reactor: a strategy for scale up, J. Chem. Eng. 400 (2020) 125875.
[18] H. Hu, Z. Wang, L. Cao, L. Zeng, C. Zhang, W. Lin, C. Wang, Metal-organic frameworks embedded in a liposome facilitate overall photocatalytic water splitting, Nat. Chem. 13 (4) (2021) 358–366.
[19] S. Zhang, J. Zhang, J. Sun, Z. Tang, Capillary microphotoreactor packed with TiO_2-coated glass beads: an efficient tool for photocatalytic reaction, Chem. Eng. Process.: Process Intensif. 147 (2020) 107746.
[20] T. Uekert, M.A. Bajada, T. Schubert, C.M. Pichler, E. Reisner, Scalable photocatalyst panels for photoreforming of plastic, biomass and mixed waste in flow, ChemSusChem 14 (19) (2021) 4190–4197.
[21] M.A. Khan, A.J. Sprockel, K.A. Macmillan, M.T. Alting, S.P. Kharal, S. Boakye-Ansah, M.F. Haase, Nanostructured, fluid-bicontinuous gels for continuous-flow liquid-liquid extraction, Adv. Mater. 34 (18) (2022) 2109547.
[22] M.F. Haase, H. Jeon, N. Hough, J.H. Kim, K.J. Stebe, D. Lee, Multifunctional nanocomposite hollow fiber membranes by solvent transfer induced phase separation, Nat. Commun. 8 (1) (2017) 1234.
[23] J.W. Tavacoli, J.H.J. Thijssen, A.B. Schofield, P.S. Clegg, Novel, robust, and versatile bijels of nitromethane, ethanediol, and colloidal silica: capsules, sub-ten-micrometer domains, and mechanical properties, Adv. Funct. Mater. 21 (11) (2011) 2020–2027.
[24] M.N. Lee, A. Mohraz, Hierarchically porous silver monoliths from colloidal bicontinuous interfacially jammed emulsion gels, J. Am. Chem. Soc. 133 (18) (2011) 6945–6947.
[25] C. Huang, J. Forth, W. Wang, K. Hong, G.S. Smith, B.A. Helms, T.P. Russell, Bicontinuous structured liquids with sub-micrometre domains using nanoparticle surfactants, Nat. Nanotechnol. 12 (11) (2017) 1060–1063.
[26] G. Vilé, D. Albani, M. Nachtegaal, Z. Chen, D. Dontsova, M. Antonietti, N. López, J. Pérez-Ramírez, A stable single-site palladium catalyst for hydrogenations, Angew. Chem. Int. Ed. 54 (38) (2015) 11265–11269.
[27] S. Mazzanti, G. Manfredi, A.J. Barker, M. Antonietti, A. Savateev, P. Giusto, Carbon nitride thin films as all-in-one technology for photocatalysis, ACS Catal. 11 (17) (2021) 11109–11116.
[28] Y. Zou, K. Xiao, Q. Qin, J.-W. Shi, T. Heil, Y. Markushyna, L. Jiang, M. Antonietti, A. Savateev, Enhanced organic photocatalysis in confined flow through a carbon nitride nanotube membrane with conversions in the millisecond regime, ACS Nano 15 (4) (2021) 6551–6561.
[29] C. Yang, R. Li, K.A.I. Zhang, W. Lin, K. Landfester, X. Wang, Heterogeneous photoredox flow chemistry for the scalable organosynthesis of fine chemicals, Nat. Commun. 11 (1) (2020) 1239.
[30] A. Sivo, V. Ruta, V. Granata, O. Savateev, M.A. Bajada, G. Vilé, Nanostructured carbon nitride for continuous-flow trifluoromethylation of (hetero)arenes, ACS Sustain. Chem. Eng. 11 (13) (2023) 5284–5292.
[31] N. Allasia, S.M. Collins, Q.M. Ramasse, G. Vilé, Hidden impurities generate false positives in single atom catalyst imaging, Angew. Chem. Int. Ed. (2024) e202404883.
[32] Z. Chen, S. Pronkin, T.-P. Fellinger, K. Kailasam, G. Vilé, D. Albani, F. Krumeich, R. Leary, J. Barnard, J.M. Thomas, J. Pérez-Ramírez, M. Antonietti, D. Dontsova, Merging single-atom-dispersed silver and carbon nitride to a joint electronic system *via* copolymerization with silver tricyanomethanide, ACS Nano 10 (3) (2016) 3166–3175.

[33] D.H. Wu, A.D. Chen, C.S. Johnson, An improved diffusion-ordered spectroscopy experiment incorporating bipolar-gradient pulses, J. Magn. Reason. A 115 (2) (1995) 260–264.
[34] Wolfram Research, Inc., Mathematica: Mathematica v14.0; Champaign, Illinois, 2022.
[35] R.J. Brandi, M.A. Citroni, O.M. Alfano, A.E. Cassano, Absolute quantum yields in photocatalytic slurry reactors, Chem. Eng. Sci. 58 (3–6) (2003) 979–985.
[36] C. Casado, J. Marugán, R. Timmers, M. Muñoz, R. van Grieken, Comprehensive multiphysics modeling of photocatalytic processes by computational fluid dynamics based on intrinsic kinetic parameters determined in a differential photoreactor, J. Chem. Eng. 310 (2017) 368–380.
[37] J. Albertazzi, F. Florit, V. Busini, R. Rota, A novel static mixer for photochemical reactions, Chem. Eng. Process.: Process Intensif. 182 (2022) 109201.
[38] J. Liu, H. Wang, M. Antonietti, Graphitic carbon nitride "reloaded": emerging applications beyond (photo)catalysis, Chem. Soc. Rev. 45 (8) (2016) 2308–2326.
[39] J. Luo, V. Ruta, I.S. Kwon, J. Albertazzi, N. Allasia, O. Nevskyi, V. Busini, D. Moscatelli, G. Vilé, Fabricating a structured single-atom catalyst *via* high-resolution photopolymerization 3D printing, Adv. Funct. Mater. 2404794 (2024).
[40] M.A. Bajada, G. Di Liberto, S. Tosoni, V. Ruta, L. Mino, N. Allasia, A. Sivo, G. Pacchioni, G. Vilé, Light-driven C-O coupling of carboxylic acids and alkyl halides over a Ni single-atom catalyst, Nat. Synth. 2 (11) (2023) 1092–1103.
[41] S. Boakye-Ansah, M.A. Khan, M.F. Haase, Controlling surfactant adsorption on highly charged nanoparticles to stabilize bijels, J. Phys. Chem. C 124 (23) (2020) 12417–12423.
[42] F. Pizzetti, A. Rossetti, A. Marchetti, F. Castiglione, V. Vanoli, E. Coste, V. Veneruso, P. Veglianese, A. Sacchetti, A. Cingolani, F. Rossi, Biphasic porous structures formed by monomer/water interface stabilization with colloidal nanoparticles, Adv. Mater. Interfaces 8 (21) (2021) 2100991.
[43] M.F. Haase, K.J. Stebe, D. Lee, Continuous fabrication of hierarchical and asymmetric bijel microparticles, fibers, and membranes by solvent transfer-induced phase separation (STRIPS), Adv. Mater. 27 (44) (2015) 7065–7071.
[44] Y. Hu, Y. Shim, J. Oh, S. Park, S. Park, Y. Ishii, Synthesis of ^{13}C-, ^{15}N-labeled graphitic carbon nitrides and NMR-based evidence of hydrogen-bonding assisted two-dimensional assembly, Chem. Mater. 29 (12) (2017) 5080–5089.
[45] M.P.F. Pepels, M.R. Hansen, H. Goossens, R. Duchateau, From polyethylene to polyester: influence of ester groups on the physical properties, Macromolecules 46 (19) (2013) 7668–7677.
[46] Q. Xiang, J. Yu, M. Jaroniec, Preparation and enhanced visible-light photocatalytic H_2-production activity of graphene/C_3N_4 composites, J. Phys. Chem. C 115 (15) (2011) 7355–7363.
[47] Y. Lv, D. Ma, K. Song, S. Mao, Z. Liu, D. He, X. Zhao, T. Yao, J.-W. Shi, Graphitic carbon nitride decorated with C-N compounds broken by *s*-triazine unit as homojunction for photocatalytic H_2 evolution, J. Mater. Chem. A Mater 11 (2) (2023) 800–808.
[48] H. Shi, H. Chi, Z. Luo, L. Jiang, X.J. Loh, C. He, Z. Li, Self-healable, fast responsive poly(*ω*-pentadecalactone) thermogelling system for effective liver cancer therapy, Front. Chem. (2019) 7.
[49] L. Urpí, A. Alla, A. Martínez de Ilarduya, Elastomeric copolyesters of *ω*-pentadecalactone and cyclohexylenedimethylene succinate obtained by enzymatic polymerization, Polymer 266 (2023) 125624.
[50] P. Groves, Diffusion ordered spectroscopy (DOSY) as applied to polymers, Polym. Chem. 8 (44) (2017) 6700–6708.
[51] M. Holz, S.R. Heil, A. Sacco, Temperature-dependent self-diffusion coefficients of water and six selected molecular liquids for calibration in accurate 1H NMR PFG measurements, Phys. Chem. Chem. Phys. 2 (20) (2000) 4740–4742.
[52] M. Krotkiewski, I.S. Ligaarden, K.-A. Lie, D.W. Schmid, On the importance of the Stokes-Brinkman equations for computing effective permeability in karst reservoirs, Commun. Comput. Phys. 10 (5) (2011) 1315–1332.
[53] X. Zhan, C. Yan, Y. Zhang, G. Rinke, G. Rabsch, M. Klumpp, A.I. Schäfer, R. Dittmeyer, Investigation of the reaction kinetics of photocatalytic pollutant degradation under defined conditions with inkjet-printed TiO_2 films – from batch to a novel continuous-flow microreactor, React. Chem. Eng. 5 (9) (2020) 1658–1670.
[54] D.D. Phan, F. Babick, M.T. Nguyen, B. Wessely, M. Stintz, Modelling the influence of mass transfer on fixed-bed photocatalytic membrane reactors, Chem. Eng. Sci. 173 (2017) 242–252.